

Uncovering distinct environments in an extended physical system around the W33 complex

L. K. Dewangan^{1*}, T. Baug², and D. K. Ojha³

¹*Physical Research Laboratory, Navrangpura, Ahmedabad - 380 009, India.*

²*Kavli Institute for Astronomy and Astrophysics, Peking University, 5 Yiheyuan Road, Haidian District, Beijing 100871, P. R. China.*

³*Department of Astronomy and Astrophysics, Tata Institute of Fundamental Research, Homi Bhabha Road, Mumbai 400 005, India.*

ABSTRACT

We present a multi-wavelength investigation of a large-scale physical system containing the W33 complex. The extended system ($\sim 50 \text{ pc} \times 37 \text{ pc}$) is selected based on the distribution of molecular gas at $[29.6, 60.2] \text{ km s}^{-1}$ and of 88 ATLASGAL $870 \mu\text{m}$ dust clumps at $d \sim 2.6 \text{ kpc}$. The extended system/molecular cloud traced in the maps of ^{13}CO and C^{18}O emission contains several H II regions excited by OB stars (age $\sim 0.3\text{--}1.0 \text{ Myr}$) and a thermally supercritical filament (“fs1”, length $\sim 17 \text{ pc}$). The filament, devoid of the ionized gas, shows dust temperature (T_d) of $\sim 19 \text{ K}$, while the H II regions are depicted with T_d of $\sim 21\text{--}29 \text{ K}$. It suggests the existence of two distinct environments in the cloud. The distribution of Class I young stellar objects (mean age $\sim 0.44 \text{ Myr}$) traces the early stage of star formation (SF) toward the cloud. At least three velocity components (around 35, 45, and 53 km s^{-1}) are investigated toward the system. The analysis of ^{13}CO and C^{18}O reveals the spatial and velocity connections of cloud components around 35 and 53 km s^{-1} . The observed positions of previously known sources, W33 Main, W33 A and O4-7I stars, are found toward a complementary distribution of these two cloud components. The filament “fs1” and a previously known object W33 B are seen toward the overlapping areas of the clouds, where ongoing SF activity is evident. A scenario concerning the converging/colliding flows from two different velocity components appears to explain well the observed signposts of SF activities in the system.

Key words: dust, extinction – H II regions – ISM: clouds – ISM: individual object (W33) – stars: formation – stars: pre-main sequence

1 INTRODUCTION

Over the past two decades, due to the availability of various large-scale multi-wavelength surveys, the research concerning the understanding of the formation processes of massive OB stars ($\gtrsim 8 M_\odot$) and young stellar clusters has received immense interest, and is being debated (Zinnecker & Yorke 2007; Tan et al. 2014). In this context, Galactic star-forming sites hosting mid-infrared (MIR) bubbles/shells associated with H II regions and/or infrared dark clouds (IRDCs)/elongated filamentary features are thought to be prime targets for exploring the highlighted research problem (e.g., Churchwell et al. 2006, 2007; André et al. 2010, 2014). The exploration of the existing multi-wavelength surveys allows to examine the physical conditions and the kinematics of embedded structures on large-scale areas of these sites,

which hold crucial clues about the birth processes of clusters of young stellar objects (YSOs) and massive stars. In this connection, the target of this paper is a massive star-forming site W33, which is located in the inner Galaxy. Previous studies have reported that W33 hosts several massive OB stars and star-forming clumps, and filaments (Westerhout 1958; Immer et al. 2013, 2014; Maud et al. 2017; Kohno et al. 2018, and references therein).

Based on the radio line and continuum observations (Downes et al. 1980; Haschick & Ho 1983; Lockman 1989; Anderson et al. 2014, 2015) and the VLT/SINFONI near-infrared (NIR) spectroscopic observations (Messineo et al. 2015), several ionized clumps/H II regions and massive OB stars have been investigated in the W33 complex (see Figure 1 in Kohno et al. 2018). In the W33 complex, Messineo et al. (2015) reported that the population of massive stars (including O4-7 type stars) formed during $\sim 2\text{--}4 \text{ Myr}$ ago. At least six dust continuum clumps at $870 \mu\text{m}$ were detected toward the W33 complex within an area of $15 \text{ pc} \times 15 \text{ pc}$ (e.g.,

* lokeshd@prl.res.in

Contreras et al. 2013), which were referred to as W33 Main, W33 A, W33 B, W33 Main1, W33 A1, and W33 B1 (see Figure 1 in Kohno et al. 2018). Kohno et al. (2018) identified two CO bipolar outflows toward W33 Main and W33 A, and the dynamical timescales of those outflows were computed to be $\sim 3 \times 10^4$ yr. Immer et al. (2013) detected water masers toward W33 A (G012.90–0.24, G012.90–0.26) and W33 Main (G012.81–0.19) in a radial velocity (V_{lsr}) range of 33–38 km s $^{-1}$, while the water masers in W33 B (G012.68–0.18) were observed in a velocity range of 57–63 km s $^{-1}$. Note that the radial velocity information has been found different for W33 B compared to W33 A and W33 Main. These authors suggested the kinematic distance of ~ 3.7 kpc (corresponding to V_{lsr} of 36 km s $^{-1}$). They also reported the parallax distance of the water masers in the massive star forming complex W33 (containing G012.68–0.18, G012.81–0.19, G012.90–0.24, G012.90–0.26) to be ~ 2.4 kpc.

It was suggested that the distance estimated using the trigonometric parallax observations of maser sources is more reliable than the kinematic distance measurements (e.g., Reid et al. 2009; Sato et al. 2010; Immer et al. 2013). Hence, despite different V_{lsr} values, it has been considered that the sites (i.e., W33 A (G012.90–0.24, G012.90–0.26), W33 B (G012.68–0.18), and W33 Main (G012.81–0.19)) are located at the similar distance, and are part of the W33 complex (e.g., Immer et al. 2013; Messineo et al. 2015; Kohno et al. 2018). Based on the detection of methanol masers, Kohno et al. (2018) also pointed out the presence of massive YSOs toward the sub-regions W33 Main, W33 A, and W33 B. Using the high-resolution molecular line data, inner environments of at least two sub-regions W33 A and W33 Main have been reported in the literature (Galván-Madrid et al. 2010; Jiang et al. 2015; Maud et al. 2017). To explain star formation (SF) activity in the direction of W33 A, Galván-Madrid et al. (2010) proposed a triggered SF scenario by filamentary convergent gas flows from two different velocity components. In the direction of the W33 complex, Kohno et al. (2018) reported three velocity components at 35, 45, and 58 km s $^{-1}$, and found the signatures of the collision between two clouds at 35 and 58 km s $^{-1}$. They assumed these clouds at a distance of ~ 2.4 kpc. Considering this argument, a collision scenario was proposed to explain the massive SF in the W33 complex (see Kohno et al. 2018, for more details). Messineo et al. (2015) also mentioned the possibility of sequential SF and feedback in W33. However, such study is not extensively carried out in W33. To our knowledge, earlier observational works toward W33 are restricted up to an area of 15 pc \times 15 pc (see Figure 1 in Kohno et al. 2018), and its large-scale environment (i.e., > 35 pc \times 35 pc) is yet to be examined.

In this context, Figure 1a displays a large-scale area ($\sim 1^\circ.1 \times 0^\circ.815$) containing the W33 complex using the ATLASGAL 870 μm dust continuum map. Figure 1a also indicates an area ($\sim 0^\circ.4 \times 0^\circ.4$) by a broken box, which was studied by Kohno et al. (2018). The locations of W33 A (G012.90–0.24, G012.90–0.26), W33 B (G012.68–0.18), and W33 Main (G012.81–0.19) are also marked by filled circles in Figure 1a. In Figure 1a, the positions of 88 ATLASGAL clumps at 870 μm (from Urquhart et al. 2018) are also marked by diamonds. Urquhart et al. (2018) obtained velocities toward the ATLASGAL clumps and also tried to compute the distance information for the clumps. All

these ATLASGAL clumps are depicted in a velocity range of [30, 56] km s $^{-1}$, and are located at a distance of ~ 2.6 kpc (Urquhart et al. 2018), which are in agreement with the previously published results (e.g., Immer et al. 2013; Kohno et al. 2018). In this paper, we have adopted a distance of ~ 2.6 kpc to the entire selected area around the W33 complex for all the analysis.

One can also notice that the ATLASGAL survey has allowed us to trace the boundary of an extended physical system hosting the W33 complex (area ~ 50 pc \times 37 pc; distance ~ 2.6 kpc; see Figure 1a). However, we do not find any study related to unearth the physical conditions and the kinematics of embedded structures on large-scale areas. In this paper, using a multi-wavelength approach, we aim to explore the ongoing physical processes in the extended physical system hosting W33. In particular, this observational work focuses to understand the formation mechanisms of massive stars and clusters of YSOs. In this connection, the study of molecular gas toward our selected extended system has been carefully carried out using the FOREST Unbiased Galactic plane Imaging survey with the Nobeyama 45-m telescope (FUGIN; Umemoto et al. 2017) $^{13}\text{CO}(J=1-0)$ and $\text{C}^{18}\text{O}(J=1-0)$ line data.

The present paper is organized as follows. The information of the adopted data sets is given in Section 2. In Section 3, we present the observational findings derived using the multi-wavelength surveys. We discuss the possible SF processes in Section 4. Finally, the main conclusions of this paper are presented in Section 5.

2 DATA SETS AND ANALYSIS

With the aid of the spatial distribution of 88 ATLASGAL clumps at a distance of ~ 2.6 kpc, the selected target area ($\sim 1^\circ.1 \times 0^\circ.815$ (or ~ 50 pc \times 37 pc); centered at $l = 12^\circ.946$; $b = -0^\circ.192$) around W33 is presented in Figure 1a. Table 1 gives a summary of various multi-wavelength survey data adopted in this paper. In the selected wide-scale area, these surveys offer to examine the distribution of H_2 column densities, dust temperatures, dust clumps, ionized gas, YSOs, and gas kinematics as well as the embedded structures/morphologies.

In order to study the gas distribution toward the selected target area, the present paper employs the molecular $^{13}\text{CO}(J=1-0)$ and $\text{C}^{18}\text{O}(J=1-0)$ line data from the FUGIN survey (Umemoto et al. 2017). In the survey, the multi-beam receiver, FOur-beam REceiver System on the 45-m Telescope (FOREST; Minamidani et al. 2016; Nakajima et al. 2019), was used for the observations. The FUGIN molecular line data are calibrated in main beam temperature (T_{mb}) (see Umemoto et al. 2017, for more details). The typical rms noise level¹ (T_{mb}) is ~ 0.7 K for both the ^{13}CO and C^{18}O lines (Umemoto et al. 2017). To improve sensitivities, we smoothed the FUGIN data cube with a Gaussian function having a half power beam width of $35''$.

¹ <https://nro-fugin.github.io/status/>

Table 1. Details of different surveys utilized in this paper.

Survey	band/line(s)	Resolution (")	Reference
NRAO VLA Sky Survey (NVSS)	21 cm	~46	Condon et al. (1998)
FUGIN survey	^{13}CO , C^{18}O ($J = 1-0$)	~20	Umemoto et al. (2017)
APEX Telescope Large Area Survey of the Galaxy (ATLASGAL)	870 μm	~19.2	Schuller et al. (2009)
<i>Herschel</i> Infrared Galactic Plane Survey (Hi-GAL)	70–500 μm	~5.8–37	Molinari et al. (2010a)
<i>Spitzer</i> MIPS Inner Galactic Plane Survey (MIPSGAL)	24 μm	~6	Carey et al. (2005)
<i>Spitzer</i> Galactic Legacy Infrared Mid-Plane Survey Extraordinaire (GLIMPSE)	3.6–8.0 μm	~2	Benjamin et al. (2003)

3 RESULTS

3.1 Wide-scale view around W33: environment and H II regions

Figure 1a exhibits the spatial distribution of 88 ATLASGAL clumps (having $d \sim 2.6$ kpc and V_{lsr} range $\sim [30, 56]$ km s^{-1}) overlaid on the ATLASGAL continuum map at 870 μm , illustrating an extended physical system as mentioned earlier. Figure 1b shows the overlay of the NVSS radio continuum emission contours on the MIPSGAL 24 μm image, revealing the locations of H II regions in our selected system. The NVSS 1.4 GHz radio continuum data suggest the presence of the ionized gas, while the warm dust emission is traced in the 24 μm image. Additionally, one can also find the absorption features against the Galactic background in the 24 μm image, revealing the IRDCs (see arrows in Figure 1b). The locations of previously identified at least three O4-7(super)-giant stars (see IDs #7, 8, and 23; from Messineo et al. 2015) are marked in Figures 1a and 1b (see filled stars). With the application of the *clumpfind* IDL program (Williams et al. 1994) in the NVSS 1.4 GHz radio continuum map, we have selected 11 ionized clumps in our target area. Figure 1c shows the boundary of each NVSS clump against the locations of earlier reported O4-7(super)-giant stars (see filled stars). A broken box is indicated in Figures 1a, 1b and 1c, which shows the area investigated by Kohno et al. (2018). The ionized clumps (see IDs #c10, #c8, and #c1–c7) are found toward the MIR bubbles (i.e., N10 and N11; Churchwell et al. 2006; Gama et al. 2016), G013.210–0.144 (White et al. 2005), and the W33 complex (W33 A (G012.90–0.24, G012.90–0.26), W33 B (G012.68–0.18), and W33 Main (G012.81–0.19); see Figure 1c), where we also find extended warm dust emission at 24 μm (see Figure 1b). Two massive O4-7(super)-giant stars (i.e., #7 and #8) are seen toward the NVSS clump #c3, while a massive O4-7(super)-giant star #23 is found in the direction of the NVSS clump #c4 (see Figure 1c).

Following the work of Dewangan et al. (2017a), we have estimated the number of Lyman continuum photons (N_{uv} ; see Panagia 1973; Matsakis et al. 1976) and the dynamical age (t_{dyn} ; see Dyson & Williams 1980) of each ionized clump (see Table 2). Previously, Kohno et al. (2018) adopted an initial particle number density of the ambient neutral gas (i.e., $n_0 = 10^4 \text{ cm}^{-3}$) in the estimations of the formation timescale of the H II regions G012.745–00.153 and G012.820–00.238, which was considered as a reasonable value for the W33 complex. Following the previous work of Kohno et al. (2018), in this paper, we compute the ages of the ionized clumps for a value of $n_0 = 10^4 \text{ cm}^{-3}$. The calculation uses the isothermal sound velocity in the ionized gas ($c_s = 11 \text{ km s}^{-1}$; Bisbas et

al. 2009), the radius of the H II region (R_{HII}), n_0 , and N_{uv} . Dynamical ages of the ionized clumps vary between $\sim 0.35 - 1.0$ Myr (see Table 2). The bubble N10 (see ID #c10 in Table 2) is found to be excited by an O9.5V–O9V star (age ~ 0.65 Myr), which is located away from the W33 complex. At least seven NVSS clumps (see IDs #c1–c7) are located toward the W33 complex (area $\sim 15 \text{ pc} \times 15 \text{ pc}$; see a broken box in Figure 1c), which contains OB stars (age $\sim 0.35 - 0.85$ Myr). More description of the analysis can be found in Dewangan et al. (2017a). The implication of the ages of these ionized clumps is discussed in Section 4.

3.2 Dust temperature and column density maps

In order to study the embedded structures in our selected target area, we have obtained the *Herschel* temperature and column density ($N(\text{H}_2)$) maps from the site². The spatial resolution of these maps is $\sim 12''$. Using the Bayesian *PPMAP* procedure operated on the *Herschel* data at wavelengths of 70, 160, 250, 350 and 500 μm (Marsh et al. 2015, 2017), the *Herschel* temperature and column density maps were produced for the *EU-funded ViaLactea project* (Molinari et al. 2010b).

In Figures 2a and 2b, we display the *Herschel* temperature and column density ($N(\text{H}_2)$) maps of our selected target area, respectively. In both the *Herschel* maps, a broken box shows the area studied by Kohno et al. (2018). The *Herschel* temperature map shows the existence of embedded structures with $T_d \sim 17-19$ K in the system, and is overlaid with a temperature contour of 18.6 K, allowing us to depict filamentary structures (see labels fs1 and fs2 in Figure 2a). The *Herschel* temperature map also exhibits extended features with $T_d \sim 21-29$ K in the direction of the previously known H II regions (see W33 A (G012.90–0.24, G012.90–0.26), W33 B (G012.68–0.18), W33 Main (G012.81–0.19), MIR bubbles, and G013.210–0.144).

In Figure 2b, the column density contour (in white) is also overlaid on the $N(\text{H}_2)$ map with a level of $3.35 \times 10^{22} \text{ cm}^{-2}$, indicating the presence of materials with high column densities. Using this $N(\text{H}_2)$ contour level, we trace the boundary of the filament “fs1” (length ~ 17 pc), which is also highlighted by a broken black curve in Figure 2b. However, an elongated morphology of filament “fs2”, as traced in the *Herschel* temperature map, is not seen by this $N(\text{H}_2)$ contour level. One of the parts of the filament “fs2” is prominently depicted by this $N(\text{H}_2)$ contour level (see a broken white circle). In the direction of the IRDCs highlighted in

² <http://www.astro.cardiff.ac.uk/research/ViaLactea/>

the image at 24 μm , both the *Herschel* maps indicate the presence of the embedded filaments. With the knowledge of T_d toward the filamentary structures and the H II regions, two distinct environments are evident in the selected physical system.

Based on the analysis of the *Herschel* column density and temperature maps, we examine the stability of the elongated filament “fs1” (mass $\sim 51000 M_\odot$; length ~ 17 pc; $T_d \sim 19$ K). To compute the mass of the filament/clump, we employed the equation, $M_{\text{area}} = \mu_{H_2} m_H \text{Area}_{\text{pix}} \Sigma N(H_2)$, where μ_{H_2} is the mean molecular weight per hydrogen molecule (i.e., 2.8), Area_{pix} is the area subtended by one pixel (i.e., $6''/\text{pixel}$), and $\Sigma N(H_2)$ is the total column density (see also Dewangan et al. 2017a). Following the works of Dewangan et al. (2018b), we have estimated the line mass or mass per unit length (i.e., $M_{\text{line,obs}} \sim 3000 M_\odot \text{pc}^{-1}$) and the critical line mass ($M_{\text{line,crit}}$) of the filament “fs1”. Due to unknown inclination angle of the filament, we consider the observed line mass as an upper limit. The expression of $M_{\text{line,crit}}$ is given by $\sim 16 M_\odot \text{pc}^{-1} \times (T_{\text{gas}}/10 \text{ K})$ for a gas filament, assuming that the filament is an infinitely extended, self-gravitating and isothermal cylinder without magnetic support (e.g. Ostriker 1964; Inutsuka & Miyama 1997; André et al. 2014). The value of $M_{\text{line,obs}}$ can be compared against the critical line mass $M_{\text{line,crit}}$ of 16–32 $M_\odot \text{pc}^{-1}$ at $T = 10$ –20 K, suggesting that the filament “fs1” is thermally supercritical. In general, the thermally supercritical filaments are believed to be unstable to radial gravitational collapse and fragmentation (e.g., André et al. 2010).

3.3 Star Formation Activities

In this section, to examine the ongoing SF activities, we have identified Class I YSOs in our selected target area around the W33 complex. In this context, the color-color plot ($[4.5] - [5.8]$ vs $[3.6] - [4.5]$) is employed (not shown here), and the infrared color conditions (i.e., $[4.5] - [5.8] \geq 0.7$ mag and $[3.6] - [4.5] \geq 0.7$ mag) are adopted to depict Class I YSOs (see Hartmann et al. 2005; Getman et al. 2007; Dewangan et al. 2017b, 2018a,c, for more details). Photometric magnitudes of point-like sources at 3.6–5.8 μm were downloaded from the *Spitzer* GLIMPSE-I Spring’07 highly reliable catalog. In this work, we considered only sources with a photometric error of less than 0.2 mag in each *Spitzer* band.

Figure 3a shows the overlay of the positions of 901 Class I YSOs on the ATLASGAL 870 μm map (see blue circles). In Figures 3b and 3c, we present surface density contours (in blue) of Class I YSOs overlaid on the ATLASGAL 870 μm dust continuum map and the NVSS 1.4 GHz radio continuum map, respectively. The surface density contours are shown with the levels of 1.2, 2, 3.5, and 6.5 YSOs/ pc^2 , where $1\sigma = 1.1$ YSOs pc^{-2} . A spatial correlation between the dust continuum emission and the Class I YSOs is also clearly seen in Figure 3b. A majority of Class I YSOs (mean age ~ 0.44 Myr; Evans et al. 2009) are seen toward the *Herschel* filaments (i.e., “fs1” and “fs2”) and the H II regions, indicating the presence of the early stage of SF in the selected physical system. The surface density analysis is performed using the nearest-neighbour (NN) method (see Casertano & Hut 1985; Gutermuth et al. 2009; Bressert et al. 2010; Dewangan et al. 2017a, for more details). Following the similar procedures as reported in Dewangan et al. (2017a), we pro-

duce the surface density map of all the selected Class I YSOs using a $15''$ grid and 6 NN at a distance of 2.6 kpc.

3.4 Kinematics of molecular gas

In Figure 4a, we display the positions of 88 ATLASGAL clumps (having $d \sim 2.6$ kpc and V_{lsr} range $\sim [30, 56]$ km s^{-1}). Figure 4b presents the distribution of V_{lsr} of 88 clumps against the Galactic longitude. In the direction of $l = 13^\circ.08$ – $13^\circ.4$, this plot suggests the presence of at least two clouds (at $[30, 41]$ km s^{-1} (or around 35 km s^{-1}) and $[48, 56]$ km s^{-1} (or around 53 km s^{-1})) containing the dust clumps. Furthermore, we also find two clumps with V_{lsr} of ~ 45 km s^{-1} toward $l \approx 13^\circ.1$. A majority of the ATLASGAL dust clumps are associated with the gas at $[30, 41]$ km s^{-1} . In the direction of our selected system, our analysis of the clumps indicates the presence of at least three velocity components. Previously, three cloud components at 35, 45, and 58 km s^{-1} were also reported toward the W33 complex (see Kohno et al. 2018). In this section, we have analyzed the FUGIN molecular line data to further explore various cloud components. In Figure 4c, we display the observed $^{13}\text{CO}(J=1-0)$ and $\text{C}^{18}\text{O}(J=1-0)$ spectra in the direction of an area highlighted by a solid box in Figure 4a), revealing two noticeable velocity peaks (i.e., 35 and 53 km s^{-1}). These profiles are produced by averaging the selected area.

In the direction of the selected target area, Figures 5a and 5b display the integrated $^{13}\text{CO}(J=1-0)$ and $\text{C}^{18}\text{O}(J=1-0)$ intensity maps, respectively. In each intensity map, the molecular gas is integrated over a velocity range of $[29.6, 60.2]$ km s^{-1} . Both the maps display an extended morphology of the molecular cloud associated with the selected target area, appearing like a giant molecular cloud (GMC).

Figure 6 presents the integrated ^{13}CO velocity channel maps (at intervals of 1.3 km s^{-1}). The distribution of ^{13}CO gas in the channel maps suggests the existence of different velocity components in the direction of the selected physical system (see panels at $[36.82, 38.12]$, $[44.62, 45.92]$, and $[53.72, 55.02]$ km s^{-1}). In Figures 7a and 7b, we show the longitude-velocity maps of ^{13}CO and C^{18}O , respectively. Both the position-velocity maps depict three velocity components around 35, 45, and 53 km s^{-1} (see arrows in Figures 7a and 7b). Similar result is also derived using the distribution of the radial velocities of the ATLASGAL clumps (see Figure 4b). In the velocity space, the cloud components around 35 and 53 km s^{-1} appear to be connected by a low-intensity intermediate velocity emission around 45 km s^{-1} (see red broken curves toward $l = 13^\circ.1$ – $13^\circ.2$ and $l = 12^\circ.7$ – $12^\circ.8$ in Figure 7a).

Based on the observed different velocity components, Figures 8a, 8c, and 8e show the spatial distribution of ^{13}CO gas associated with the clouds at $[29.6, 43.3]$, $[44, 46.5]$, and $[47.2, 60.2]$ km s^{-1} , respectively. In Figures 8b, 8d, and 8f, we present the distribution of C^{18}O gas associated with the clouds at $[29.6, 43.3]$, $[44, 46.5]$, and $[47.2, 60.2]$ km s^{-1} , respectively. In each panel of Figure 8, the positions of W33 A, W33 B, and W33 Main are also highlighted by open circles, while the positions of three O4–7I stars (see IDs #7, 8, and 23 in Messineo et al. 2015) are shown by filled stars (in cyan). The sites W33 A and W33 Main are seen with the highest intensities in the ^{13}CO and C^{18}O maps at $[29.6, 43.3]$ km s^{-1} , while the corresponding areas are seen with

low intensities in the ^{13}CO and C^{18}O maps at $[47.2, 60.2]$ km s^{-1} . One can find a very weak ^{13}CO and C^{18}O emission toward W33 B in the cloud at $[29.6, 43.3]$ km s^{-1} , while the strong molecular emission is traced toward W33 B in the cloud at $[47.2, 60.2]$ km s^{-1} . In the direction of the filamentary structures and the W33 complex, some areas with compact ^{13}CO and C^{18}O emission are also seen in map at $[44, 46.5]$ km s^{-1} , which is an intermediate velocity range between other two clouds.

In Figure 9a, we show a color-composite image of our selected area with the ^{13}CO maps at $[29.6, 43.3]$ and $[47.2, 60.2]$ km s^{-1} in red and green, respectively. The filamentary feature “fs1” observed in the *Herschel* column density map and the positions of the ATLASGAL clumps are also highlighted in Figure 9a. Figure 9b displays the overlay of the surface density of Class I YSOs on the color-composite image produced using the ^{13}CO maps at $[29.6, 43.3]$ and $[47.2, 60.2]$ km s^{-1} . A majority of the Class I YSOs are found toward the common zones of the two cloud components (see areas toward the filamentary structures and the W33 complex). In Figure 9c, we present the overlay of the NVSS 1.4 GHz radio continuum contours on the color-composite image produced using the C^{18}O maps at $[29.6, 43.3]$ and $[47.2, 60.2]$ km s^{-1} . Both the color-composite images allow us to infer the overlapping zones of the two clouds at $[47.2, 60.2]$ and $[29.6, 43.3]$ km s^{-1} , where the early phase of SF, dust clumps as well as H II regions are evident. Furthermore, in the color-composite images, a spatial fit of the intensity-depression region and the intensity-enhancement region is observed toward the W33 complex (see also Figure 10). In the direction of the W33 complex, an intensity-enhancement is found in the molecular intensity maps at $[29.6, 43.3]$ km s^{-1} (see Figures 10a and 10b), while an intensity-depression region or cavity-like feature is observed in the molecular intensity maps at $[47.2, 60.2]$ km s^{-1} (see Figures 10c and 10d). The locations of W33 A (G012.90–0.24, G012.90–0.26), W33 Main (G012.81–0.19), and three O4–7I stars (see IDs #7, 8, and 23 in Messineo et al. 2015) are seen toward the areas of the spatial fit of the cavity and the intensity-enhancement region. However, the filament “fs1” and W33 B are found toward the common zones of the two clouds.

Overall, the study of the molecular line data shows the spatial and velocity connections of two cloud components in the direction of the selected physical system. We have discussed these results in more details in Section 4.

4 DISCUSSION

4.1 Physical environment around W33

As highlighted earlier, previously published results were mainly focused to the H II regions associated with the W33 complex (area $\sim 15 \text{ pc} \times 15 \text{ pc}$; see a broken box in Figures 1a and 1b). The large-scale environment around the W33 complex is not yet studied and explored. Such study can enable us to obtain new insights in the target site and to infer different physical mechanism(s) than earlier studies on small-scale environment. The present paper deals with an extended physical system ($\sim 50 \text{ pc} \times 37 \text{ pc}$), which is investigated by the distribution of 88 ATLASGAL clumps located at a distance of $\sim 2.6 \text{ kpc}$. It is also confirmed by

the distribution of molecular gas at $[29.6, 60.2]$ km s^{-1} , and at least three velocity components (around 35, 45, and 53 km s^{-1}) are identified in the direction of our selected physical system (see Section 3.4). The physical system is found to host the embedded filaments (i.e., fs1 and fs2) and several H II regions. The filaments are not associated with any radio continuum emission, and exhibit T_d of ~ 17 – 19 K . In our selected system, a relatively warm dust emission ($T_d \sim 21$ – 29 K) is also found toward the H II regions excited by OB-type stars (see Table 2). These results together show the existence of two distinct environments in the selected physical system, which differ substantially in their dust temperatures (see Section 3.2). The elongated filament (“fs1”; length $\sim 17 \text{ pc}$; $T_d \sim 19 \text{ K}$) is characterized as a thermally supercritical filament, and appears to be on the verge of collapse (see Section 3.2). Based on the distribution of Class I YSOs (mean age $\sim 0.44 \text{ Myr}$; Evans et al. 2009), the early phase of SF activities is investigated toward the filaments and the H II regions (age ~ 0.35 – 1.0 Myr) in the system (see Section 3.3).

4.2 Star Formation Scenarios

Considering the presence of multiple velocity components and massive O-type stars, one can explore the applicability of the triggered SF scenarios concerning the expansion of H II regions (e.g., Elmegreen & Lada 1977; Bertoldi 1989; Whitworth et al. 1994; Lefloch & Lazareff 1994; Elmegreen 1998; Deharveng et al. 2005; Dale et al. 2007; Bisbas et al. 2015; Walch et al. 2015; Kim et al. 2018; Haid et al. 2019) and the colliding/converging flows from two velocity components (Ballesteros-Paredes et al. 1999; Heitsch et al. 2008; Vázquez-Semadeni et al. 2007) or the collision of two clouds (Elmegreen 1998). Massive OB-stars are the important sources of mechanical and radiative energy, and can impact their surroundings through their intense energetic feedback (i.e., stellar wind, ionized emission, and radiation pressure). However, the stellar feedback cannot explain the existence of multiple velocity components in the selected physical system (see also Kohno et al. 2018).

Concerning the “cloud cloud collision” (CCC) process, Habe & Ohta (1992) studied numerical simulations of a head-on collision of two non-identical clouds. The simulations develop gravitationally unstable cores/clumps at the interface of the clouds due to the effect of their compression. In the CCC process, young stellar clusters and massive stars can be formed at the intersection of two molecular clouds or the shock-compressed interface layer (e.g., Habe & Ohta 1992; Ananthpindika 2010; Inoue & Fukui 2013; Takahira et al. 2014; Haworth et al. 2015a,b; Torii et al. 2017; Bisbas et al. 2017, and references therein). In the CCC site, one may observationally find the spatial and velocity connections of two molecular clouds (e.g., Torii et al. 2017; Dewangan 2017; Dewangan & Ojha 2017; Dewangan et al. 2017b, 2018a, 2019). In the position-velocity map, one may also trace bridging features between two molecular clouds, which enable us to infer the association of the two clouds (e.g., Haworth et al. 2015a,b). It may also hint the presence of a compressed layer of gas due to two colliding clouds/flows (e.g., Haworth et al. 2015a,b; Torii et al. 2017). Furthermore, one may also observe a complementary spatial distribution of two clouds in the CCC site (e.g., Torii et al. 2017;

Fukui et al. 2018; Dewangan et al. 2018c, 2019), which is related to the spatial fit of “Key/intensity-enhancement” and “Cavity/Keyhole/intensity-depression” features.

In the direction of the W33 complex (area ~ 15 pc \times 15 pc; see a broken box in Figures 1a and 1b), Kohno et al. (2018) proposed the CCC model to explain the formation of massive stars. They found complementary distributions of two clouds (at 35 and 58 km s $^{-1}$) around the W33 complex. These authors also computed the timescale of the collision between these two clouds (i.e., 0.7–1.0 Myr), which was found to be older than the dynamical timescales of the outflows in W33 Main and W33 A (i.e., $\sim 10^4$ yr; Kohno et al. 2018). They concluded that the sources in the W33 complex (i.e., W33 Main, W33 A, W33 B, W33 Main1, W33 A1, and W33 B1) were formed in the dense layer produced via the collision event. One can note that previously, no attempt was made to examine the wide-area around the W33 complex, which has been carefully carried out in the present paper.

In the present work, we have detected three velocity components around 35, 45, and 53 km s $^{-1}$ toward our selected physical system. Kohno et al. (2018) reported the cloud at 58 km s $^{-1}$ as the third velocity component using the NANTEN2 ^{12}CO ($J = 1-0$) emission. It appears that the cloud at 53 km s $^{-1}$ reported in this paper is a part of the cloud component at 58 km s $^{-1}$ identified by Kohno et al. (2018) (see Figure 2b in their paper). In the direction of the W33 complex and the filamentary structures, in the velocity space, the two clouds around 35 and 53 km s $^{-1}$ are linked by lower intensity intermediate velocity emission, which may trace bridge-like features around 45 km s $^{-1}$ (see broken curves around $l = 12^\circ.8$ and $l = 13^\circ.1$ in Figure 7a). An analysis of the spatial distribution of molecular gas associated with two clouds around 35 and 53 km s $^{-1}$ shows the overlapping areas toward the filament “fs1” and W33 B (see arrows in Figure 9a). These overlapping areas are ablaze with SF activities including massive stars (see Figures 9b and 9c), where we also find materials with high column densities.

Additionally, a complementary distribution of two clouds (around 35 and 53 km s $^{-1}$) is evident toward the W33 complex (see Figures 10a & 10c, and 10b & 10d), where the objects W33 Main, W33 A, and three massive O-type stars (i.e., #7, #8, and #23) are located. As mentioned earlier, the complementary distribution of clouds was also reported by Kohno et al. (2018). The key-like or intensity-enhancement feature is traced in the cloud at [29.6, 43.3] km s $^{-1}$ (or around 35 km s $^{-1}$), while the key-hole or cavity-like feature is evident in the cloud at [47.2, 60.2] km s $^{-1}$ (or around 53 km s $^{-1}$). However, we do not find any signature of complementary distribution of two clouds in the direction of the filament “fs1” and W33 B, but these objects are seen toward the common zones of the two clouds as discussed above. Overall, these results suggest the interaction of the two cloud components around 35 and 53 km s $^{-1}$ toward our selected physical system, which is associated with the early phase of SF activities and hosts H II regions powered by massive OB stars. Note that our findings can be considered as an extension of the published work of Kohno et al. (2018), but for a larger region or area (i.e., ~ 50 pc \times 37 pc). They reported the timescale of the collision to be 0.7–1.0 Myr.

In Figure 10e, we display the overlay of the Scutum and Norma arms (from Reid et al. 2016) on the longitude-

velocity map of ^{13}CO . The radial velocities of 88 ATLASGAL clumps are also shown in Figure 10e. Figure 10e also provides the information of the near side of the Norma and Scutum arms as well as the far side of the Scutum arm. Previously, based on the parallax measurements of maser sources, it was reported that the W33 complex is located toward the Scutum arm (see Figure 3 in Sato et al. 2014). Considering the distribution of the molecular gas and the ATLASGAL clumps in the velocity space, one may examine the interaction or collision of the gas clouds associated with the Scutum arm.

Earlier, using high resolution continuum and line data from the Submillimeter Array (SMA) and the Very Large Array (VLA) facilities, Galván-Madrid et al. (2010) studied the SF activity toward W33 A, and interpreted observed results in W33 A through a triggered SF scenario by filamentary convergent gas flows from two different velocity components (see also Inoue et al. 2018). In this scenario, one can expect the origin of molecular clouds via the convergence of streams of neutral gas. With time, the merging/converging/collision of the molecular clouds, filaments of molecular gas is expected, which produces the birth of cores and stars (Hunter et al. 1986; Ballesteros-Paredes et al. 1999; Vázquez-Semadeni et al. 2007; Heitsch et al. 2008; Inoue et al. 2018).

Previously, in the case of Orion Nebula Cluster (Fukui et al. 2018) and RCW 38 (Fukui et al. 2016), it was suggested that low-mass cluster members were formed before the onset of the collision event. However, in our selected target site, Class I YSOs (i.e., age ~ 0.44 Myr) and H II regions (age $\sim 0.35 - 0.85$ Myr) appear relatively younger than the collision timescale (i.e., 0.7–1.0 Myr) as reported by Kohno et al. (2018). Additionally, it was also pointed out that colliding gas flows may also lead to the birth of low-mass stars in regions of compressed gas and dust (Hunter et al. 1986).

Taking into account the detection of Class I YSOs (i.e., age ~ 0.44 Myr) and H II regions (age $\sim 0.35 - 0.85$ Myr) toward the common zones of the two cloud components around 35 and 53 km s $^{-1}$, the SF history seems to be explained by a triggered SF scenario by converging/colliding flows from two velocity components in our selected system. One can also keep in mind that the site G013.210–0.144 and the MIR bubbles (N10 and N11) appear away from the overlapping areas of the clouds. Hence, SF activities toward these objects are unlikely induced by the converging flows.

5 SUMMARY AND CONCLUSIONS

In this paper, to understand SF mechanisms, we have investigated a large-scale physical system hosting massive star-forming site W33 using a multi-wavelength approach. The present work is benefited with the analysis of the existing large-scale survey data at different wavelengths. The important results of this work are presented below.

- A spatial spread of 88 ATLASGAL 870 μm dust clumps at $d \sim 2.6$ kpc and the distribution of molecular gas at [29.6, 60.2] km s $^{-1}$ are utilized to select the extended physical system (~ 50 pc \times 37 pc).
- The information concerning the location and the radial velocity indicates our selected physical system in the direction of the Scutum and Norma arms.

- Two distinct environments are investigated in the physical system, which are embedded filaments (with $T_d \sim 17\text{--}19\text{ K}$) and H II regions powered by OB stars (with $T_d \sim 21\text{--}29\text{ K}$; age $\sim 0.3\text{--}1.0\text{ Myr}$). The filaments are not associated with any ionized emission.
- An elongated filament (“fs1”; length $\sim 17\text{ pc}$) is found to be a thermally supercritical filament.
- Based on the distribution of Class I YSOs (mean age $\sim 0.44\text{ Myr}$; Evans et al. 2009), the early stage of SF activities is observed toward the filaments and H II regions in the cloud.
- The FUGIN ^{13}CO and C^{18}O line data trace three velocity components (around 35, 45, and 53 km s^{-1}) in the direction of the system.
- The analysis of the molecular line data confirms the spatial and velocity connections of cloud components around 35 and 53 km s^{-1} .
- The positions of W33 Main, W33 A and O4-7I stars are found toward a complementary distribution of cloud components around 35 and 53 km s^{-1} .
- The spatial distribution of the clouds around 35 and 53 km s^{-1} reveals overlapping zones toward the filament “fs1” and an object W33 B, where a majority of the ATLASGAL clumps and noticeable Class I objects are depicted.

We conclude that the observed SF signposts seem to be explained well by a triggered SF scenario by converging/colliding flows from two velocity components around 35 and 53 km s^{-1} in the physical system hosting two distinct environments (i.e., H II regions and filamentary structures).

ACKNOWLEDGMENTS

We thank the anonymous reviewer for several useful comments and suggestions. The research work at Physical Research Laboratory is funded by the Department of Space, Government of India. This work is based [in part] on observations made with the *Spitzer* Space Telescope, which is operated by the Jet Propulsion Laboratory, California Institute of Technology under a contract with NASA. This publication makes use of data from FUGIN, FOREST Unbiased Galactic plane Imaging survey with the Nobeyama 45-m telescope, a legacy project in the Nobeyama 45-m radio telescope. TB is supported by the National Key Research and Development Program of China through grant 2017YFA0402702. TB also acknowledges support from the China Postdoctoral Science Foundation through grant 2018M631241. DKO acknowledges the support of the Department of Atomic Energy, Government of India, under project No. 12-R&D-TFR-5.02-0200.

REFERENCES

- Anathpindika S. V., 2010, *MNRAS*, 405, 1431
- Anderson L. D., Bania T. M., Balser D. S., Cunningham V., Wenger T. V., Johnstone B. M., Armentrout W. P., 2014, *ApJS*, 212, 1
- Anderson L. D., Armentrout W. P., Johnstone B. M., Bania T. M., Balser D. S., Wenger T. V., Cunningham V., 2015, *ApJS*, 221, 26
- André P. et al., 2010, *A&A*, 518, L102
- André P., Di Francesco J., Ward-Thompson D., Inutsuka S. -I., Pudritz R. E., Pineda J. E., 2014, in *Protostars and Planets VI*, ed. H. Beuther et al. (Tucson, AZ; Univ. Arizona Press), 27
- Ballesteros-Paredes J., Hartmann L., Vázquez-Semadeni E., 1999, *ApJ*, 527, 285
- Benjamin R. A. et al., 2003, *PASP*, 115, 953
- Bertoldi F., 1989, *ApJ*, 346, 735
- Bisbas T. G., Wünsch R., Whitworth A. P., Hubber D. A., 2009, *A&A*, 497, 649
- Bisbas T. G. et al., 2015, *MNRAS*, 453, 1324
- Bisbas T. G., Tanaka K. E. I., Tan J. C., Wu B., Nakamura F., 2017, *ApJ*, 850, 23
- Bressert E. et al., 2010, *MNRAS*, 409, 54
- Carey S. J. et al., 2005, *BAAS*, 37, 1252
- Casertano S., Hut P., 1985, *ApJ*, 298, 80
- Churchwell E. et al., 2006, *ApJ*, 649, 759
- Churchwell E. et al., 2007, *ApJ*, 670, 428
- Condon J. J., Cotton W. D., Greisen E. W., Yin Q. F., Perley R. A., Taylor G. B., Broderick J. J., 1998, *AJ*, 115, 1693
- Contreras Y. et al., 2013, *A&A*, 549, 45
- Dale J. E., Clark P. C., Bonnell I. A., 2007, *MNRAS*, 377, 535
- Deharveng L., Zavagno A., Caplan J., 2005, *A&A*, 433, 565
- Dewangan L. K., 2017, *ApJ*, 837, 44
- Dewangan L. K., Ojha D. K., 2017, *ApJ*, 849, 65
- Dewangan L. K., Ojha D. K., Zinchenko I., Janardhan P., Luna, A., 2017a, *ApJ*, 834, 22
- Dewangan L. K., Ojha D. K., Zinchenko I., 2017b, *ApJ*, 851, 140
- Dewangan L. K., Ojha D. K., Zinchenko I., Baug T., 2018a, *ApJ*, 861, 19
- Dewangan L. K., Baug T., Ojha D. K., Zinchenko I., Luna A., 2018b, *ApJ*, 864, 54
- Dewangan L. K., Dhanya J. S., Ojha D. K., Zinchenko, I., 2018c, *ApJ*, 866, 20
- Dewangan L. K., Sano H., Enokiya R., Tachihara K., Fukui Y., Ojha, D. K., 2019, *ApJ*, 878, 26
- Downes D., Wilson T. L., Bieging J., Wink J., 1980, *A&A*, 40, 379
- Dyson J. E., Williams D. A., 1980, *Physics of the interstellar medium* (New York, Halsted Press, p. 204)
- Elmegreen B. G., Lada C. J., 1977, *ApJ*, 214, 725
- Elmegreen B. G., 1998, in *ASP Conf. Ser. 148, Origins*, ed. C. E. Woodward, J. M. Shull, & H. A. Thronson, Jr. (San Francisco, CA: ASP), 150
- Evans N. J. et al., 2009, *ApJS*, 181, 321
- Fukui Y. et al., 2016, *ApJ*, 820, 26
- Fukui Y. et al., 2018, *ApJ*, 859, 166
- Getman K. V., Feigelson E. D., Garmire G., Broos P., Wang J., 2007, *ApJ*, 654, 316
- Galván-Madrid R., Zhang Q., Keto E., Ho P. T. P., Zapata L. A., Rodríguez L. F., Pineda J. E., Vázquez-Semadeni E., 2010, *ApJ*, 725, 17
- Gama D. R. G., Lepine J. R. D., Mendoza E., Wu Y., Yuan J., 2016, *ApJ*, 830, 57
- Gutermuth R. A., Megeath S. T., Myers P. C., Allen L. E., Pipher J. L., Fazio G. G., 2009, *ApJS*, 184, 18

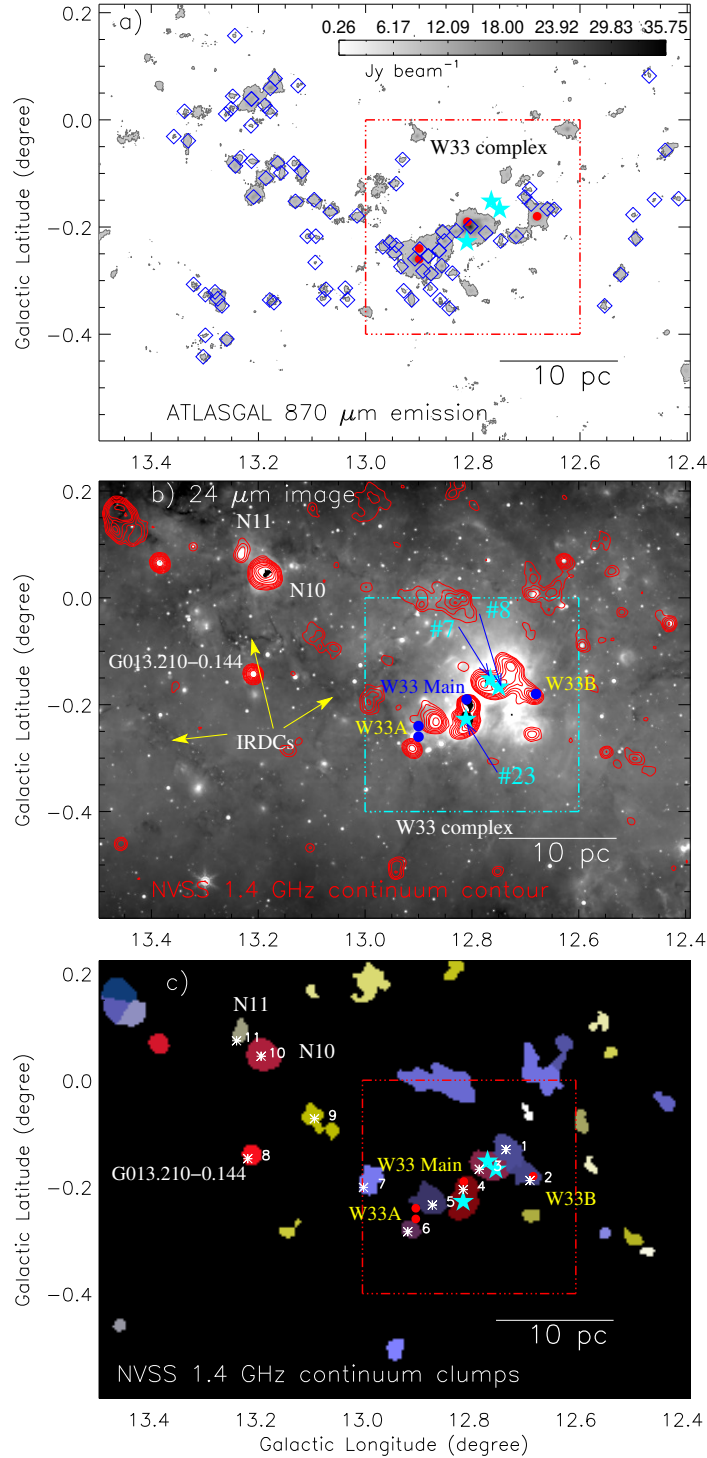


Figure 1. a) Overlay of 88 ATLASGAL dust continuum clumps at 870 μm (from Urquhart et al. 2018) on the ATLASGAL contour map at 870 μm (area $\sim 1^\circ.1 \times 0^\circ.815$ ($\sim 50 \text{ pc} \times 37 \text{ pc}$ at a distance of 2.6 kpc); central coordinates: $l = 12^\circ.946$; $b = -0^\circ.192$). The ATLASGAL contour levels are $36.48 \text{ Jy/beam} \times (0.0072, 0.012, 0.03, 0.05, 0.067, 0.08, 0.1, 0.15, 0.2, 0.25, 0.3, 0.4, 0.5, 0.6, 0.7, 0.8, 0.9, 0.95, \text{ and } 0.98)$. The ATLASGAL clumps (at $d \sim 2.6 \text{ kpc}$) are shown by blue diamonds. b) Overlay of the NVSS 1.4 GHz continuum emission contours (in red) on the MIPS GAL 24 μm image. The NVSS radio continuum contour levels are 4.7, 9.4, 18.8, 37.7, 62.8, 85.0, 156.9, 251.0, 367.5, and 1255.10 mJy beam^{-1} . The locations of G013.210-0.144, bubbles N10 and N11 as well as IRDCs are indicated in the figure. c) The boundary of selected radio clump in the NVSS 1.4 GHz radio continuum map is shown along with its corresponding ID and position (see asterisks and also Table 2). In each panel, filled stars (in cyan) show the locations of O4-7 type stars (from Messineo et al. 2015) and filled circles highlight some sub-regions in the W33 complex (i.e., W33 A (G012.90-0.24, G012.90-0.26), W33 B (G012.68-0.18), and W33 Main (G012.81-0.19)). In all the panels, the scale bar refers to 10 pc, and a broken box covering the field around the W33 complex presents the area investigated by Kohno et al. (2018).

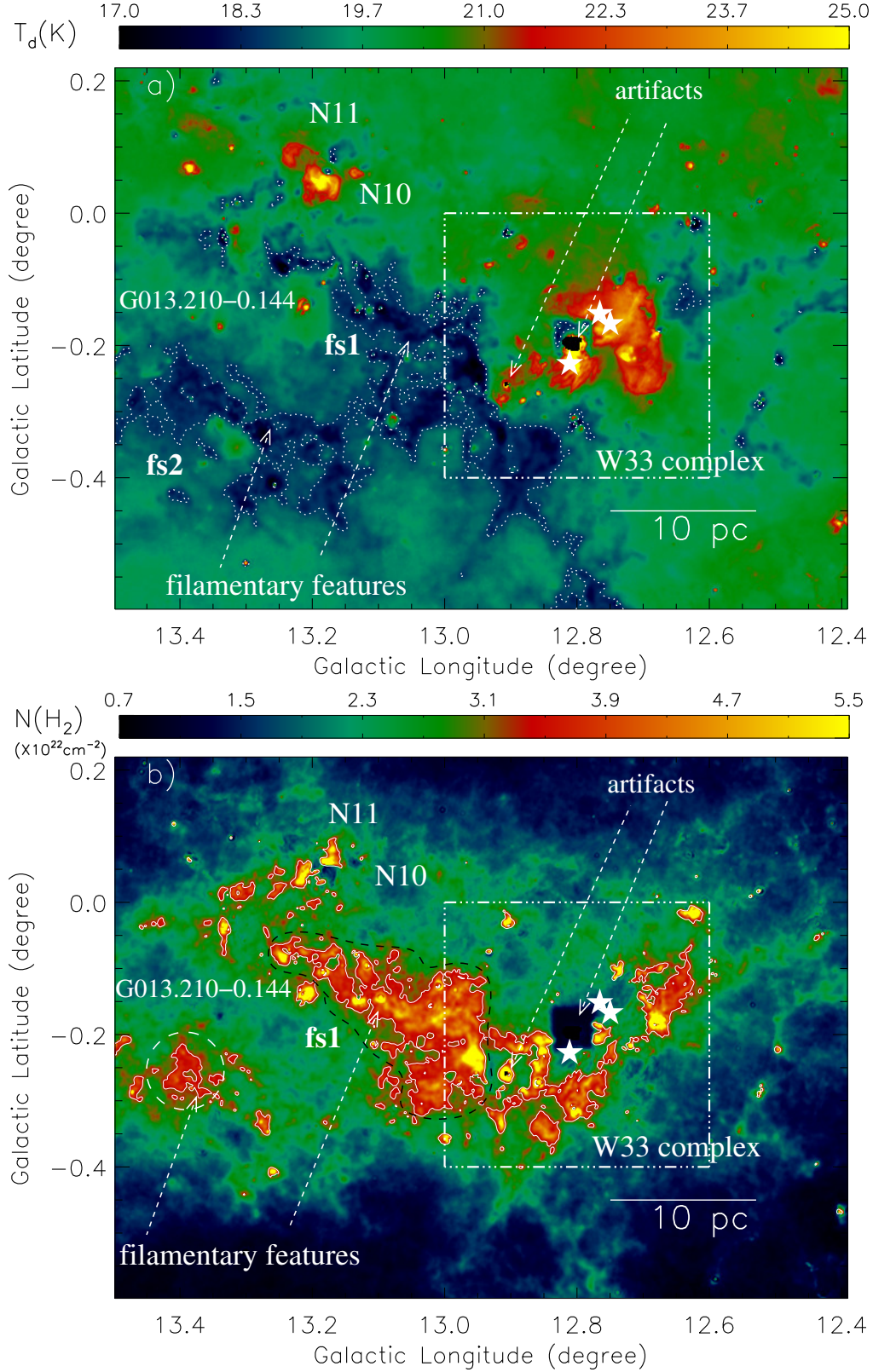


Figure 2. a) The panel shows the *Herschel* temperature map of the selected area around W33. A broken contour (in white) shows the temperature feature at 18.6 K in the figure, tracing at least two filamentary features (i.e., “fs1” and “fs2”). b) The panel shows the *Herschel* column density ($N(\text{H}_2)$) map of the selected area. The column density contour (in white) is also overlaid on the map with a level of $3.35 \times 10^{22} \text{ cm}^{-2}$. The filament “fs1” is indicated by a broken curve (in black). In each panel, the scale bar refers to 10 pc, and a broken box covering the field around the W33 complex presents the area investigated by Kohno et al. (2018). In both the panels, artifacts are also indicated by arrows, and filled stars (in white) show the locations of O4-7 type stars (see Figure 1b).

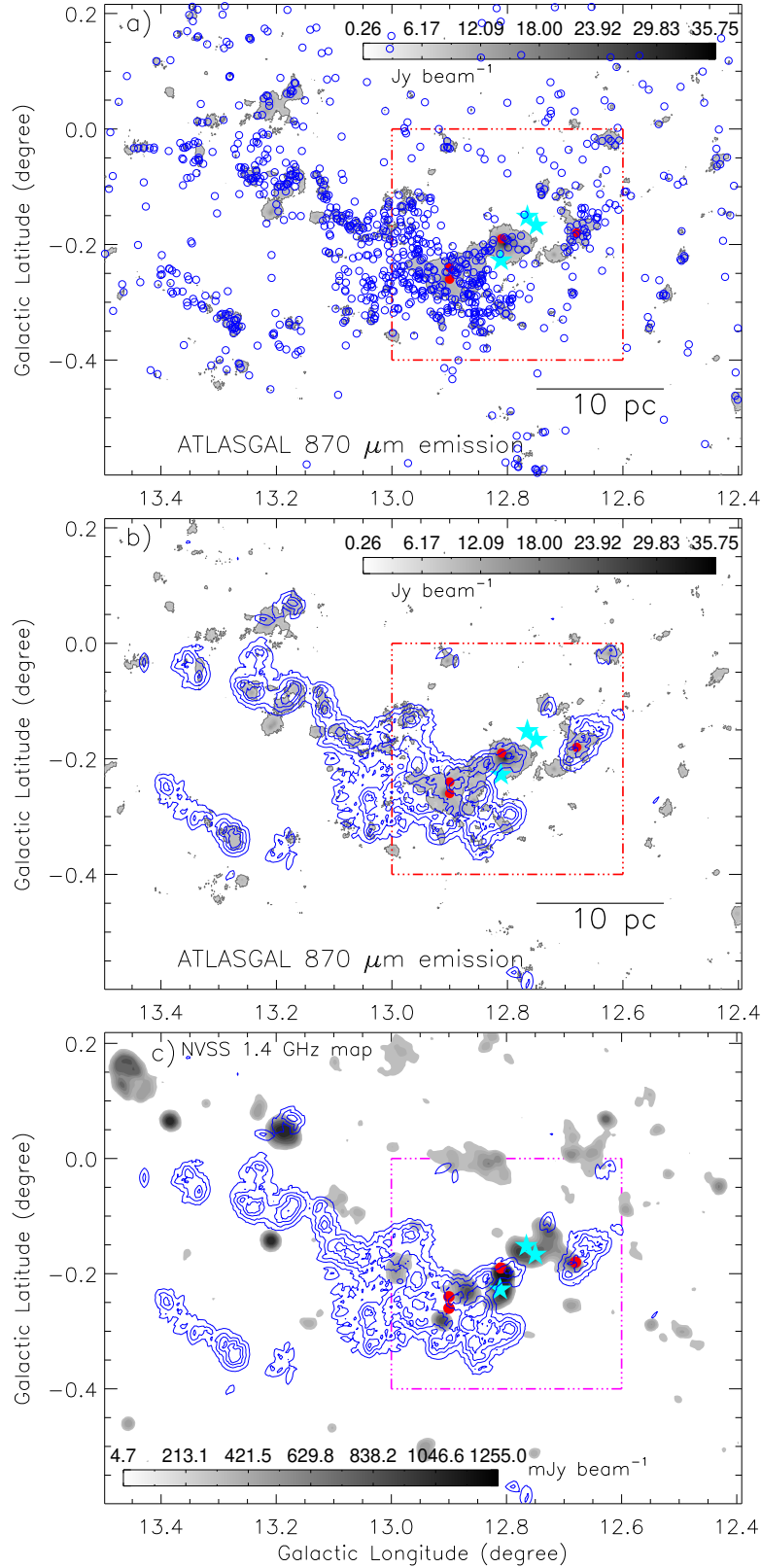


Figure 3. a) Overlay of the positions of the selected Class I YSOs on the ATLASGAL contour map at 870 μm . These YSOs (see open circles) satisfy the color conditions, $[4.5] - [5.8] \geq 0.7$ and $[3.6] - [4.5] \geq 0.7$ (see text for more details). b) The panel shows the overlay of the surface density contours (in blue) of YSOs on the ATLASGAL contour map at 870 μm . The surface density contours (in cyan) of Class I YSOs are shown with the levels of 1.2, 2, 3.5, and 6.5 YSOs/ pc^2 . c) Overlay of the surface density contours (in blue) on the NVSS 1.4 GHz continuum contour map. The ATLASGAL continuum map and the NVSS 1.4 GHz emission map are the same as in Figures 1a and 1b, respectively. In each panel, the other symbols (i.e., filled stars and filled circles) are the same as in Figure 1b.

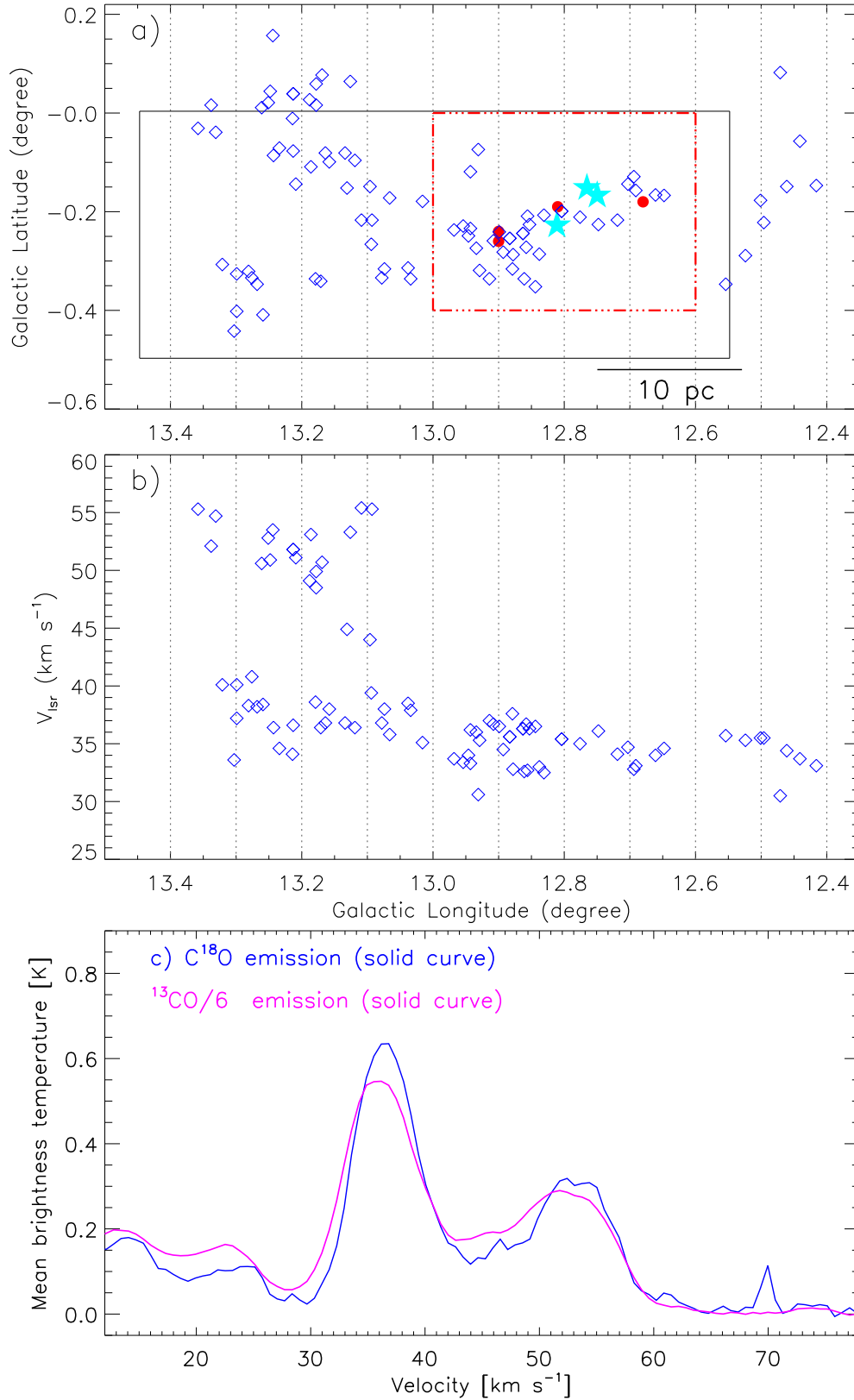


Figure 4. a) The panel displays the spatial distribution of the ATLASGAL 870 μm dust continuum clumps (see diamonds) toward the selected site (see also Figure 1a). Filled stars (in cyan) show the locations of O4-7 type stars, and filled circles (in red) highlight some sub-regions in the W33 complex (see Figure 1b). b) The panel shows the distribution of the radial velocity against the Galactic longitude (see text for more details). c) The panel shows the FUGIN ^{13}CO spectrum (see magenta curve) and the FUGIN C^{18}O spectrum (see blue curve). The profiles are produced by averaging the area highlighted by a solid box in Figure 4a. The FUGIN ^{13}CO spectrum has been divided by a factor of 6.

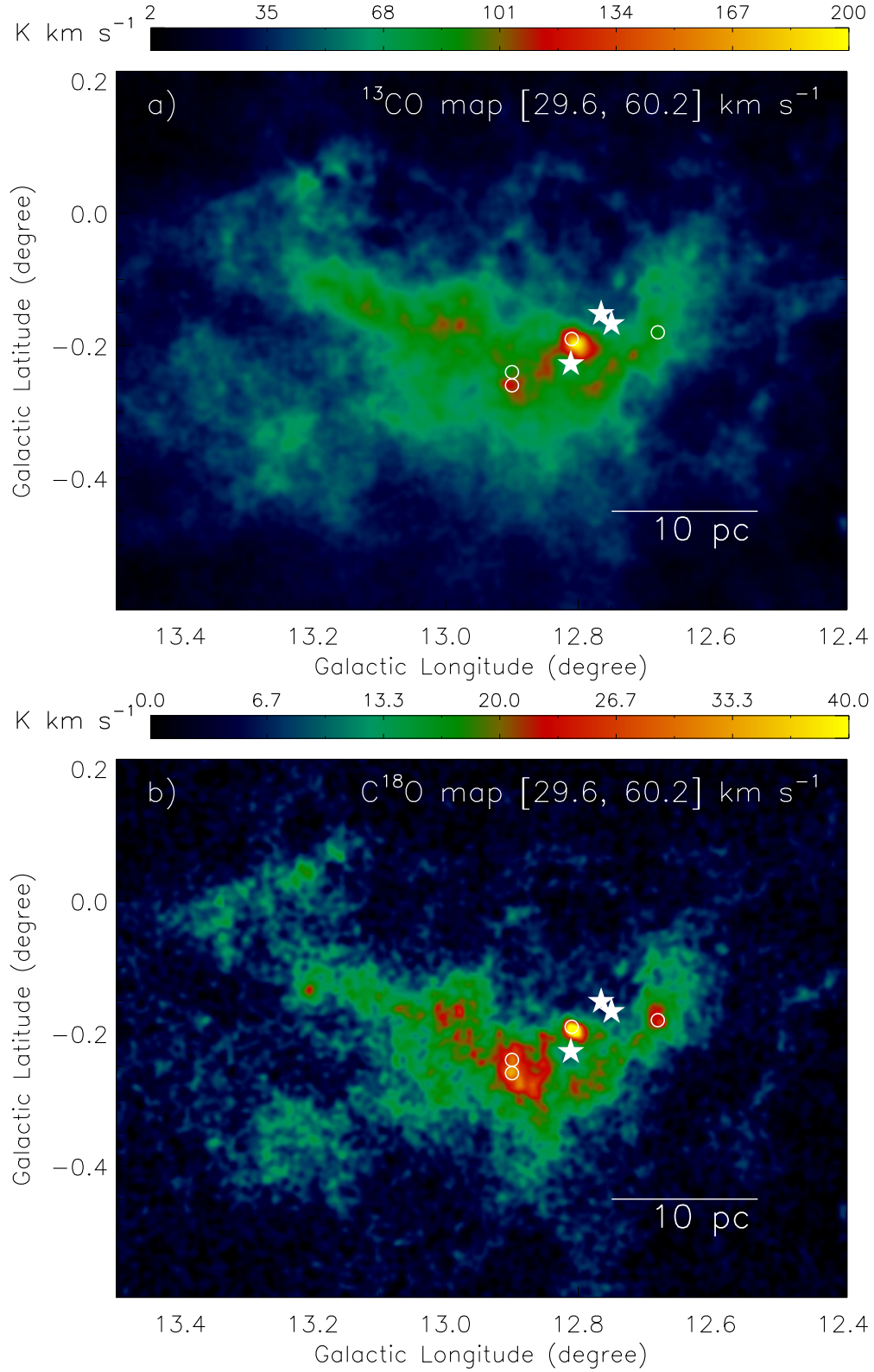


Figure 5. a) FUGIN $^{13}\text{CO}(J=1-0)$ map of intensity (moment-0) in the direction of the selected area around W33. b) FUGIN $\text{C}^{18}\text{O}(J=1-0)$ map of intensity (moment-0). In each panel, the molecular emission is integrated from 29.6 to 60.2 km s^{-1} , and a scale bar corresponding to 10 pc is shown. In each panel, filled stars (in white) show the locations of O4-7 type stars and open circles (in white) highlight some sub-regions in the W33 complex (see Figure 1b).

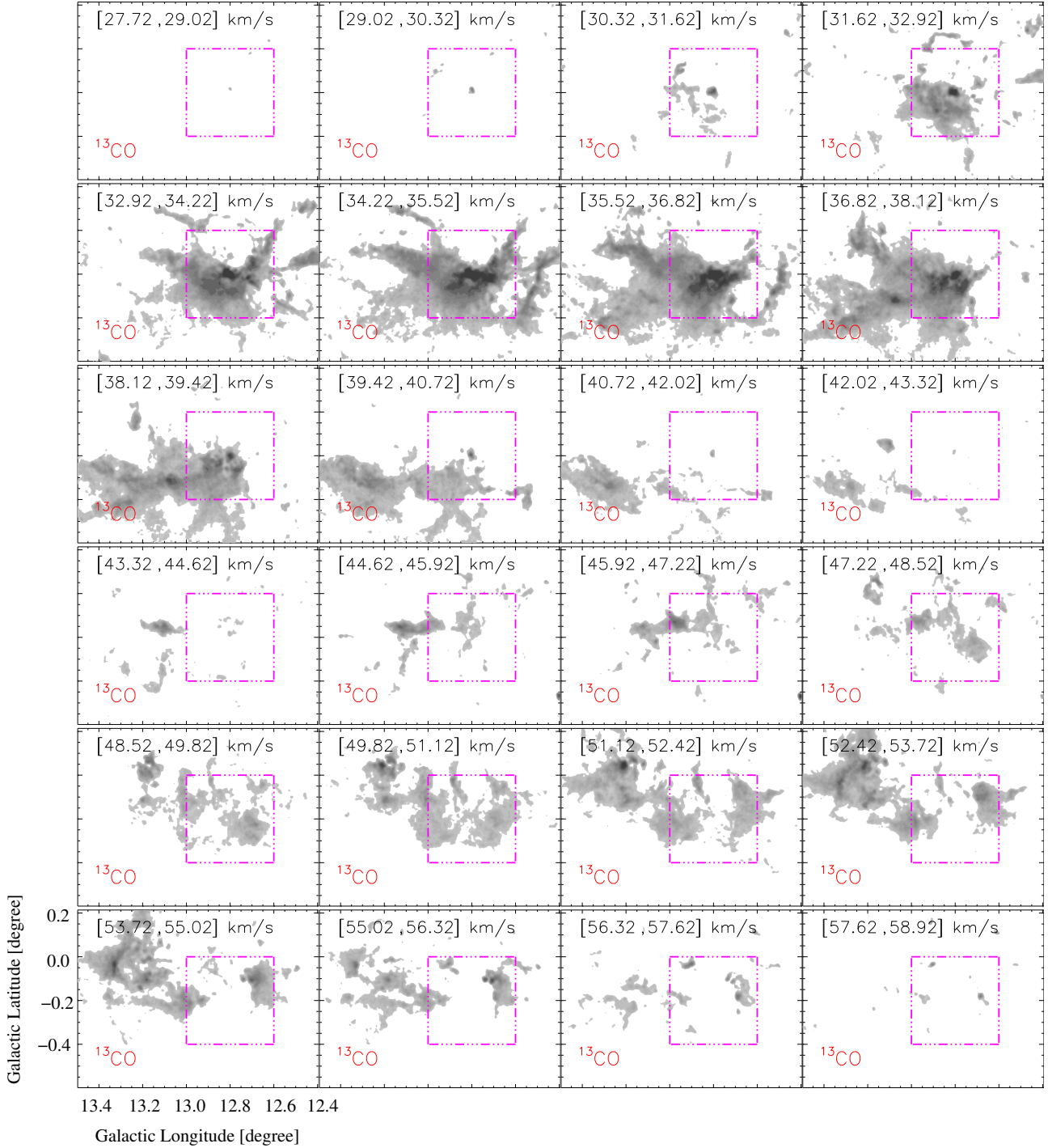


Figure 6. The integrated velocity channel maps of $^{13}\text{CO}(J=1-0)$ (at velocity intervals of 1.3 km s^{-1}). The ^{13}CO contours are shown with the levels of 4.5, 5, 6, 7, 8, 9, 10, 11, 13, 15, 18, 21, and 23 K km s^{-1} . In each panel a broken box, covering the field around the W33 complex, presents the area studied by Kohno et al. (2018).

Haschick A. D., Ho P. T. P., 1983, *ApJ*, 267, 638
Habe A., Ohta K., 1992, *PASJ*, 44, 203
Haid S., Walch S., Seifried D., Wünsch R., Dinnbier F., Naab T., 2019, *MNRAS*, 482, 4062
Hartmann L., Megeath S. T., Allen L., Luhman K., Calvet N., D'Alessio P., Franco-Hernandez R., Fazio G. G., 2005, *ApJ*, 629, 881
Haworth T. J. et al., 2015a, *MNRAS*, 450, 10

Haworth T. J., Shima K., Tasker E. J., Fukui Y., Torii K., Dale J. E., Takahira K., Habe A., 2015b, *MNRAS*, 454, 1634
Heitsch F., Hartmann L. W., Slyz A. D., Devriendt J. E.G., Burkert A., 2008, *ApJ*, 674, 316
Hunter J. H., Jr., Sandford M. T., II, Whitaker R. W., Klein R. I., 1986, *ApJ*, 305, 309
Inoue T., Fukui Y., 2013, *ApJL*, 774, 31

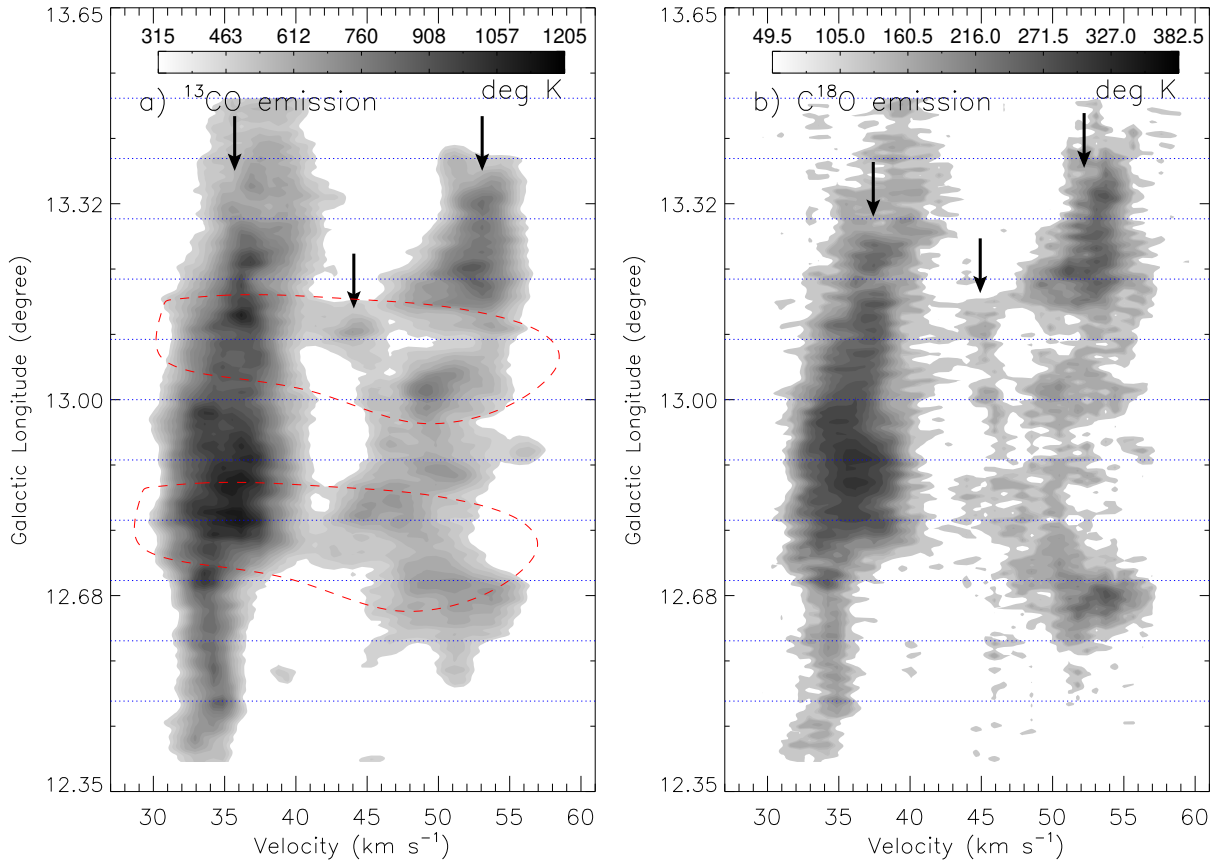


Figure 7. a) Longitude-velocity map of ^{13}CO . The contour levels are $0.45 \text{ deg K} \times (700, 800, 900, 1000, 1100, 1200, 1300, 1400, 1500, 1600, 1700, 1800, 1900, 2000, 2100, 2200, 2300, 2400, 2500, 2600, \text{ and } 2680)$. Two broken curves (in red) show the connection of different cloud components. b) Longitude-velocity map of C^{18}O . The contour levels are $0.45 \text{ deg K} \times (110, 150, 160, 170, 210, 240, 270, 300, 330, 360, 400, 440, 500, 600, 700, 800, \text{ and } 850)$. Arrows indicate three velocity components in the direction of the selected area around W33. In each panel, the molecular emission is integrated over the latitude range from $-0^\circ.6$ to $0^\circ.21$.

Table 2. Physical parameters of radio clumps traced in the NVSS 1.4 GHz continuum map (see Figure 1c). Table tabulates ID, Galactic coordinates (l , b), deconvolved effective radius of the H II region (R_{HII}), total flux (S_ν), Lyman continuum photons ($\log N_{\text{uv}}$), dynamical age (t_{dyn}), and radio spectral type.

ID	l (degree)	b (degree)	R_{HII} (pc)	S_ν (Jy)	$\log N_{\text{uv}}$ (s^{-1})	t_{dyn} (Myr) for $n_0 = 10^4 \text{ cm}^{-3}$	Spectral Type (V)
c1	12.731	-0.130	1.31	688.81	47.56	0.79	B0.5-B0
c2	12.686	-0.188	1.08	361.55	47.28	0.66	B0.5-B0
c3	12.781	-0.167	1.39	1477.56	47.89	0.72	B0-O9.5
c4	12.811	-0.205	1.53	11370.76	48.78	0.51	O7.5-O7
c5	12.869	-0.234	1.34	653.54	47.54	0.83	B0.5-B0
c6	12.915	-0.284	0.81	361.55	47.28	0.39	B0.5-B0
c7	12.998	-0.201	1.12	163.63	46.94	0.86	B0.5-B0
c8	13.215	-0.147	0.87	888.69	47.67	0.36	B0-O9.5
c9	13.090	-0.072	1.16	92.10	46.69	1.05	B0.5-B0
c10	13.190	0.045	1.43	2698.41	48.16	0.65	O9.5-O9
c11	13.236	0.074	0.80	76.43	46.61	0.57	B0.5-B0

Inoue T., Hennebelle P., Fukui Y., Matsumoto T., Iwasaki K., Inutsuka S., 2018, PASJ, 70, S53

Immer K., Reid M. J., Menten K. M., Brunthaler A., Dame T. M., 2013, A&A, 553, A117

Immer K., Galván-Madrid R., König C., Liu H. B., Menten K. M., 2014, A&A, 572, A63

Inutsuka S., Miyama S. M., 1997, ApJ, 480, 681

Jiang X. J., Liu H. B., Zhang Q., Wang J., Zhang Zhi-Yu, Li J., Gao Y., Gu, Q., 2015, ApJ, 808, 114

Kim Jeong-Gyu, Kim Woong-Tae, Ostriker E. C., 2018, ApJ, 859, 68

Kohno M. et al., 2018, PASJ, 70, S50

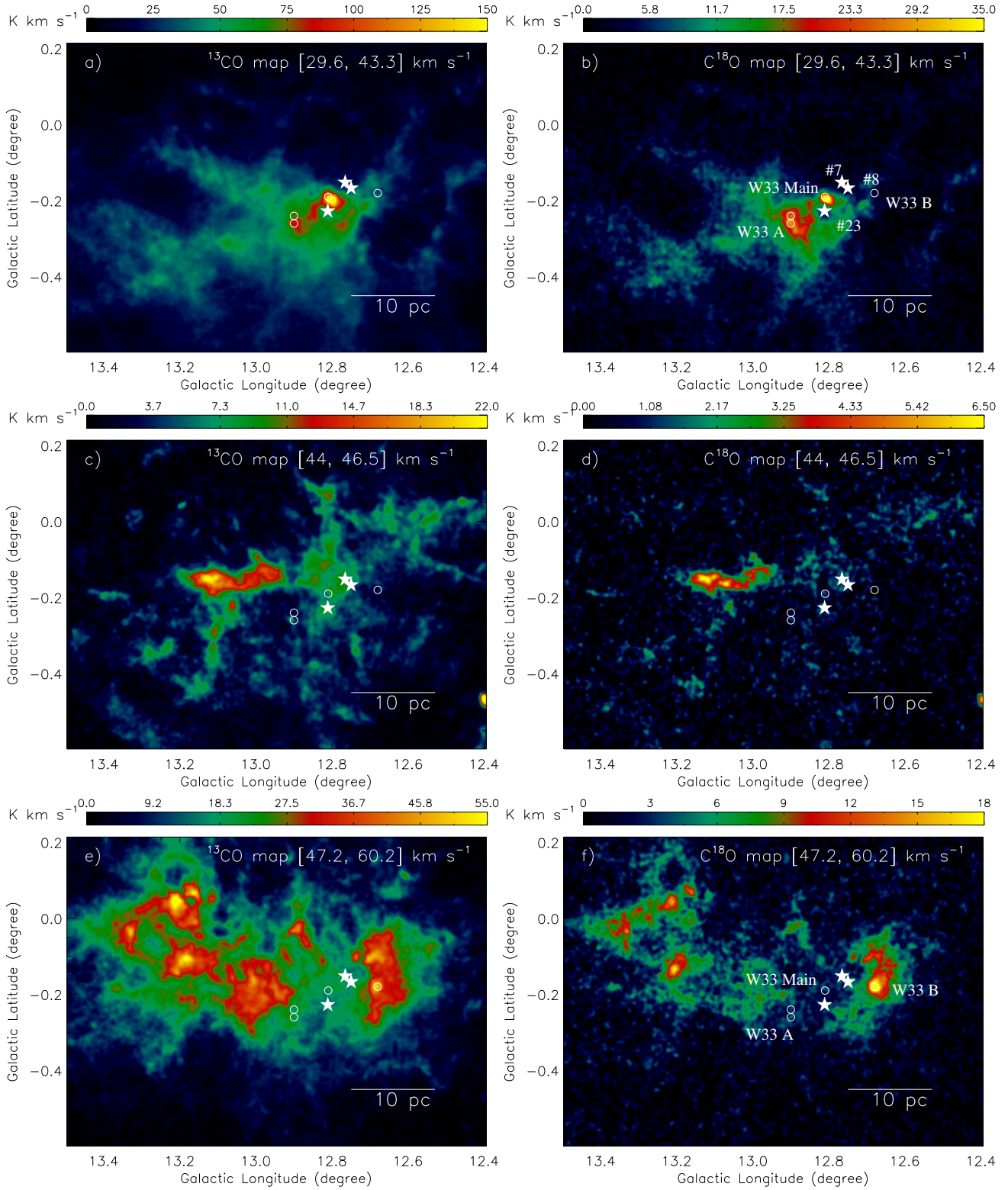


Figure 8. a) FUGIN $^{13}\text{CO}(J=1-0)$ map of intensity integrated from 29.6 to 43.3 km s^{-1} . b) FUGIN $\text{C}^{18}\text{O}(J=1-0)$ map at [29.6, 43.3] km s^{-1} . c) FUGIN $^{13}\text{CO}(J=1-0)$ map of intensity integrated from 44 to 46.5 km s^{-1} . d) FUGIN $\text{C}^{18}\text{O}(J=1-0)$ map at [44, 46.5] km s^{-1} . e) FUGIN $^{13}\text{CO}(J=1-0)$ map at [47.2, 60.2] km s^{-1} . f) FUGIN $\text{C}^{18}\text{O}(J=1-0)$ map at [47.2, 60.2] km s^{-1} . In each panel, the other symbols are the same as in Figure 1b.

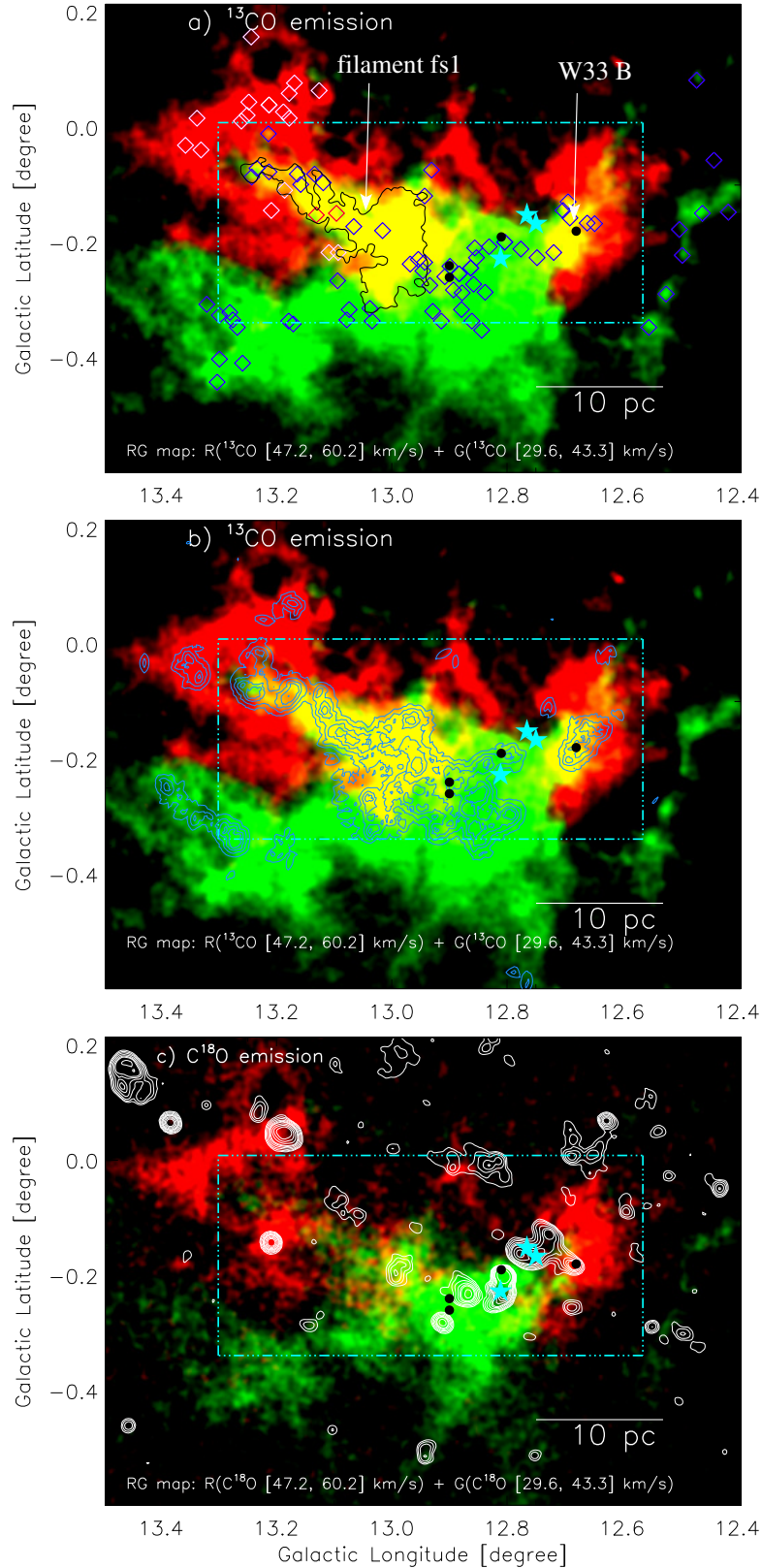


Figure 9. a) Two color-composite image produced using the ^{13}CO maps at $[47.2, 60.2]$ and $[29.6, 43.3]$ km s $^{-1}$ in red and green, respectively. The positions of the ATLASGAL 870 μm dust continuum clumps are marked by diamonds. Different colors show the clumps with different velocity ranges (i.e., white diamonds $[48.5, 55.4]$ km s $^{-1}$; red diamonds $[44.0, 44.9]$ km s $^{-1}$; blue diamonds $[30.5, 40.8]$ km s $^{-1}$). The filament “fs1” is indicated by a solid curve (in black), which is traced by the $N(\text{H}_2)$ contour of 3.35×10^{22} cm $^{-2}$ (see Figure 2b). b) Overlay of the surface density contours on the color composite map, which is the same as in Figure 9a. The surface density contours (in cyan) of Class I YSOs are shown with the levels of 1.2, 2, 3.5, and 6.5 YSOs/pc 2 . c) Overlay of the NVSS radio continuum contours (in white) on the color composite map, which is the same as in Figure 9a but for C^{18}O . The NVSS radio continuum contours are the same as in Figure 1b. In each panel, the other symbols are the same as in Figure 1b.

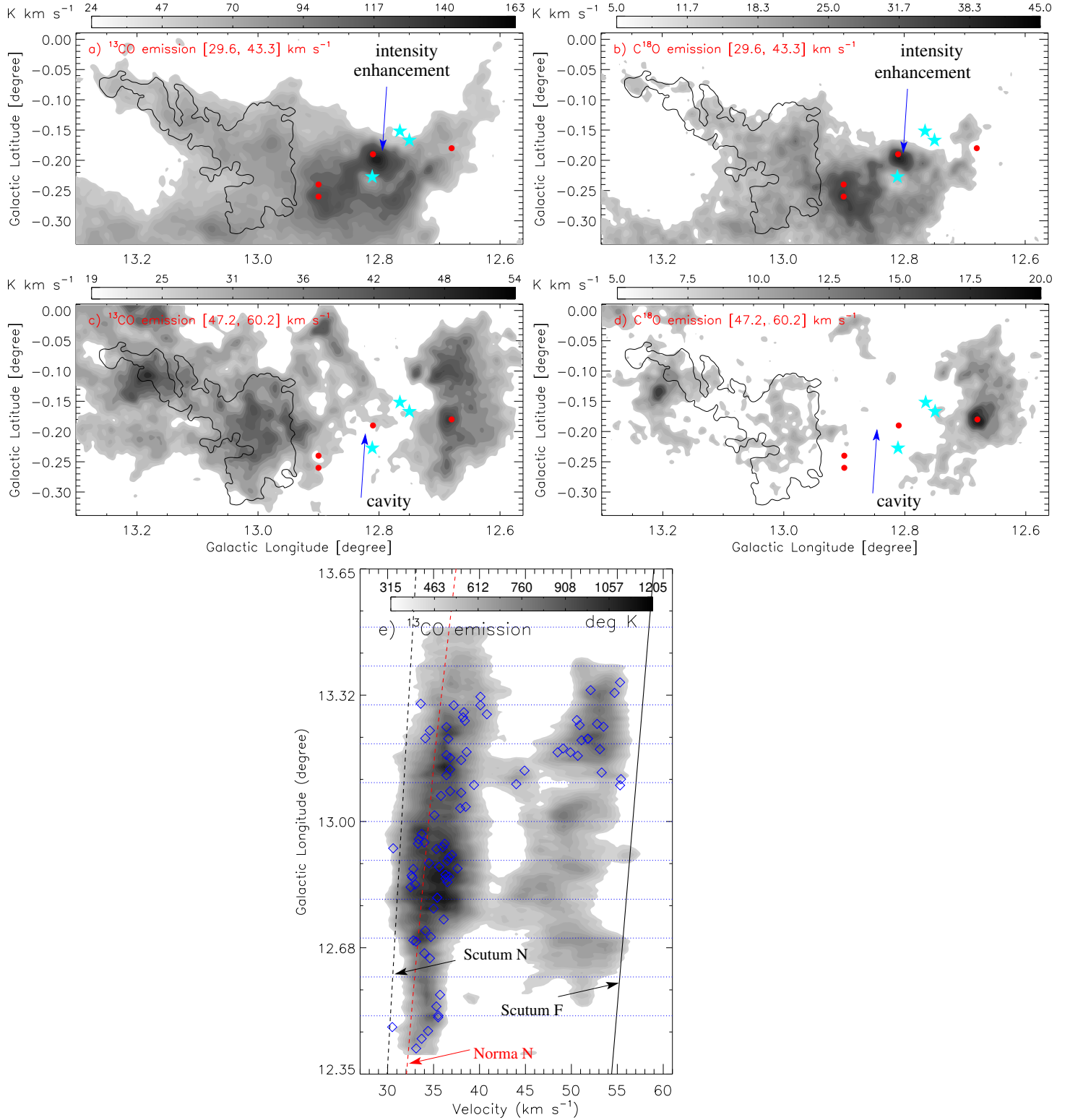


Figure 10. Distribution of molecular gas toward an area as highlighted by a broken box in Figure 9a. a) FUGIN $^{13}\text{CO}(J=1-0)$ map of intensity integrated from 29.6 to 43.3 km s^{-1} . b) FUGIN $\text{C}^{18}\text{O}(J=1-0)$ map at [29.6, 43.3] km s^{-1} . c) FUGIN $^{13}\text{CO}(J=1-0)$ map at [47.2, 60.2] km s^{-1} . d) FUGIN $\text{C}^{18}\text{O}(J=1-0)$ map of intensity integrated from 47.2 to 60.2 km s^{-1} . e) The panel exhibits the overlay of the Scutum and Norma arms (from Reid et al. 2016) on the longitude-velocity map of ^{13}CO . The near and far sides of the arms are marked by broken and solid curves, respectively. The radial velocity of each ATLASCAL clump against its longitude is also presented in the plot (see diamonds in Figure 1a). In the panels “a–d”, the other symbols are the same as in Figure 1b. In the panels “a–d”, the filament “fs1” is indicated by a solid curve (in black), which is traced by the $N(\text{H}_2)$ contour of $3.35 \times 10^{22} \text{ cm}^{-2}$ (see Figure 2b).

- Lefloch B., Lazareff B., 1994, *A&A*, 289, 559
- Lockman F. J., 1989, *ApJS*, 71, 469
- Marsh K. A., Whitworth A. P., Lomax O., 2015, *MNRAS*, 454, 4282
- Marsh K. A. et al., 2017, *MNRAS*, 471, 2730
- Matsakis D. N., Evans N. J., II, Sato T., Zuckerman B., 1976, *AJ*, 81, 172
- Maud L. T., Hoare M. G., Galván-Madrid R., Zhang Q., de Wit W. J., Keto E., Johnston K. G., Pineda J. E., 2017, *MNRAS*, 467, 120
- Messineo M. et al., 2015, *ApJ*, 805, 110
- Minamidani T. et al., 2016, Development of the new multi-beam 100 GHz band SIS receiver FOR-EST for the Nobeyama 45-m Telescope. p. 99141Z, doi:10.1117/12.2232137
- Molinari S. et al., 2010a, *A&A*, 518, L100
- Molinari S. et al., 2010b, *PASP*, 122, 314
- Nakajima T., Inoue H., Fujii Y., Miyazawa C., Iwashita H., Sakai T., Noguchi T., Mizuno A., 2019, *PASJ*, 71, 17
- Ostriker J., 1964, *ApJ*, 140, 1056
- Panagia N., 1973, *AJ*, 78, 929
- Reid M. J., Dame T. M., Menten K. M., Brunthaler A., 2016, *ApJ*, 823, 77
- Reid M. J. et al., 2009, *ApJ*, 700, 137
- Sato M., Hirota T., Reid M. J., Honma, M., Kobayashi H., Iwadate K., Miyaji T., Shibata K. M., 2010, *PASJ*, 62, 287
- Sato M. et al., 2014, *ApJ*, 793, 72
- Schuller F. et al., 2009, *A&A*, 504, 415
- Takahira K., Tasker E. J., Habe A., 2014, *ApJ*, 792, 63
- Tan J. C., Beltrán M. T., Caselli P., Fontani F., Fuente A., Krumholz M. R., McKee C. F., Stolte A., 2014, in *Protostars and Planets VI*, ed. H. Beuther et al. (Tucson, AZ: Univ. Arizona Press), 149
- Torii K. et al., 2017, *ApJ*, 835, 142
- Urquhart J. S. et al., 2018, *MNRAS*, 437, 1059
- Umemoto T. et al., 2017, *PASJ*, 69, 78
- Vázquez-Semadeni E., Gómez G. C., Jappsen A. K., Ballesteros-Paredes J., González R. F., Klessen R. S., 2007, *ApJ*, 657, 870
- Walch S., Whitworth A. P., Bisbas T. G., Hubber D. A., Wunsch R., 2015, *MNRAS*, 452, 2794
- Westerhout G., 1958, *Bull. Astron. Inst. Netherlands*, 14, 215
- Whitworth A. P., Bhattal A. S., Chapman S. J., Disney M. J., Turner J. A., 1994, *MNRAS*, 268, 291
- White R. L., Becker R. H., Helfand D. J., 2005, *AJ*, 130, 586
- Williams J. P., de Geus E. J., Blitz L., 1994, *ApJ*, 428, 693
- Zinnecker H., Yorke H. W., 2007, *ARA&A*, 45, 481